Cement and Concrete Composites 97 (2019) 279–287

Contents lists available at ScienceDirect

Cement and Concrete Composites

journal homepage: www.elsevier.com/locate/cemconcomp

Insights into the physical and chemical properties of a cement-polymer composite developed for geothermal wellbore applications

Kenton A. Rod[a], Manh-Thuong Nguyen[b], Mohamed Elbakhshwan[c,1], Simerjeet Gills[c,**,1], Barbara Kutchko[d], Tamas Varga[e], Adriana M. Mckinney[e], Timothy J. Roosendaal[a], M. Ian Childers[a], Chonghang Zhao[f,1], Yu-chen Karen Chen-Wiegart[f,g,1], Juergen Thieme[g,1], Phillip K. Koech[a], Wooyong Um[h], Jaehun Chun[a], Roger Rousseau[b], Vassiliki-Alexandra Glezakou[b], Carlos A. Fernandez[a,*]

[a] Energy and Environment Directorate, Pacific Northwest National Laboratory, Richland, WA, USA
[b] Physical and Computational Sciences Directorate, Pacific Northwest National Laboratory, Richland, WA, USA
[c] Nuclear Science and Technology Department, Brookhaven National Laboratory, Brookhaven, NY, USA
[d] National Environmental Technology Laboratory, Pittsburg, PA, USA
[e] Environmental and Molecular Sciences Laboratory, Pacific Northwest National Laboratory, Richland, WA, USA
[f] Department of Materials Science and Chemical Engineering, Stony Brook University, USA
[g] National Synchrotron Light Source II, Brookhaven National Laboratory, USA
[h] Pohang University of Science and Technology (POSTECH), Pohang, South Korea

ARTICLE INFO

Keywords:
Cement
Polymer
Geothermal
Wellbore
Self-healing

ABSTRACT

To isolate injection and production zones from overlying formations and aquifers during geothermal operations, cement is placed in the annulus between well casing and the formation. However, wellbore cement eventually undergoes fractures due to chemical and physical stress with the resulting time and cost intensive production shutdowns and repairs. To address this difficult problem, a polymer-cement (composite) with self-healing properties was recently developed by our group. Short-term thermal stability tests demonstrated the potential of this material for its application in geothermal environments. In this work, the authors unveil some of the physical and chemical properties of the cement composite in an attempt to better understand its performance as compared to standard cement in the absence of the polymer. Among the properties studied include material's elemental distribution, mineral composition, internal microstructure, and tensile elasticity. Polymer-cement composites have relatively larger, though not interconnected, levels of void spaces compared to conventional cement. Most of these void spaces are filled with polymer. The composites also seem to have higher levels of uncured cement grains as the polymer seems to act as a retarder in the curing process. The presence of homogeneously-distributed more flexible polymer in the cement brings about 60–70% higher tensile elasticity to the composite material, as confirmed experimentally and by density-functional calculations. The improved tensile elasticity suggests that the composite materials can outperform conventional cement under mechanical stress. In addition, calculations indicate that the bonding interactions between the cement and polymer remain stable over the range of strain studied. The results suggest that this novel polymer-cement formulation could represent an important alternative to conventional cement for application in high-temperature subsurface settings.

1. Introduction

The sealing of wellbores used for oil, gas, and geothermal heat production is a major environmental and practical concern. Cementing is used to fill the annulus between the geologic formation and the wellbore casing [1], with the intent to hydraulically isolate the production and injections zones the wellbore penetrates. The result contributes to preventing contamination of aquifers and surface waters,

* Corresponding author.
** Corresponding author.
E-mail addresses: gills@bnl.gov (S. Gills), Carlos.Fernandez@pnnl.gov (C.A. Fernandez).
[1] these authors contributed equally to this work.

https://doi.org/10.1016/j.cemconcomp.2018.12.022
Received 22 June 2018; Received in revised form 8 October 2018; Accepted 25 December 2018
Available online 31 December 2018
0958-9465/

extending the lifetime of the wellbore and, as a result, increasing the production efficiency. Leak risk can limit the development of clean energy alternatives, for example, there are large geothermal energy reserves in the United States and around the globe that are not in use to date due to the need of advanced technologies to make its production viable [2]. This is partially due to the failure of the wellbore cement used in geothermal wells caused by the high temperature (up to 400 °C) and chemically corrosive (typically hypersaline, CO_2 and H_2S rich) environments [3]. Failure of wellbore seals necessitates expensive and time intensive production shutdowns and repairs. With improvements in wellbore cement technologies, geothermal energy has the potential to be a sustainable energy source, which can deliver significant energy with minimal carbon release to the atmosphere.

Both inorganic and organic cement formulations have been developed to be deployed for geothermal wellbore operations but although they have high compressive strength, they tend to have low tensile strength and are vulnerable to cracking [4–6]. There has been advancement for development of self-healing cement for geothermal wellbore applications, but their physical attributes can be limited especially with respect to multiple fracturing events and separation from casing and/or formation [7,8]. Additionally, self-healing polymer-cement blends developed for the oil and gas industry often have poor mechanical properties and cannot withstand the high-temperature environments found in geothermal wells [9–17]. Therefore, the development of a self-healing polymer-cement composite which is functional in geothermal environments could represent a game-changing technology towards the growth of the geothermal energy industry.

A self-healing polymer has been developed by the authors and details of its healing mechanisms and proof of ability to heal fractures has recently been published [18,19]. In brief, this research demonstrated that on fractured surfaces, the polymer strongly anchors through hydrogen bonding and ionic Ca—O bonds which results from the deprotonation of polymer hydroxyl groups while the polymer S—S groups are turned away from the cement – polymer interface, thus allowing for the self-healing function within the polymer [19]. Fracture apertures as large as 0.3–0.5 mm were self-healed resulting in a permeability reduction of up to 87% when the novel polymer was present in the cement composite (Fig. 1) [18].

The objective of this paper was to investigate this novel self-healing cement-polymer composite further to learn about the elemental distribution, mineral composition and internal microstructure of the composite and how the material's characteristics influence its mechanical performance, specifically the tensile elasticity. To do so, the authors performed a series of tests on cement-polymer composites and compared the results to the results obtained when performing the same tests on conventional cement in the absence of polymer. These tests included scanning electron microscopy-energy dispersive X-ray spectroscopy (SEM-EDS), X-ray fluorescence (XRF) spectroscopy, X-ray microtomography (XMT), specific surface area analysis, compressive strength and Young's modulus analysis. This study demonstrates that this novel cement-polymer composite appears to be a more ductile material which can outperform conventional cement under mechanical stress. The homogeneous distribution of self-healing polymer throughout the cement matrix demonstrated in this work is the main reason for the recently reported self-healing behavior [18]. Both, ductility and autonomous healing, makes this cement-polymer composite a significant alternative material to conventional cement for application in geothermal wellbores.

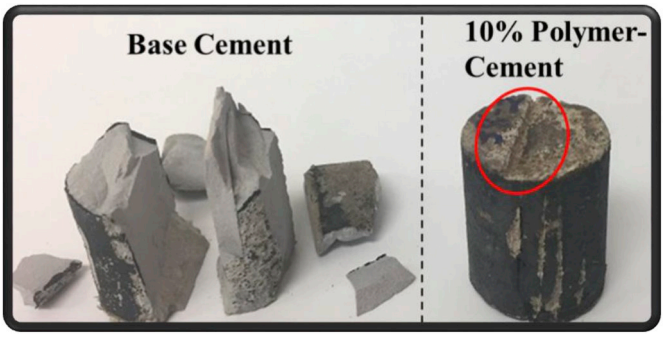

Fig. 1. Pictures of control (base cement) and composite cement taken after a healing event of a shear fracture. Note how more brittle base cement is irreversibly damaged in several pieces.

2. Methods

2.1. Cement synthesis

Class H cement was supplied by LaFarge from the Joppa Plant. Silica flour (200 mesh) was obtained from U.S. Silica. Thioplast EPS 25 (EPS 25; 0.373 of total polymer) (640 g/1 equivalent epoxide) was supplied by Akzo Nobel, and poly(ethylene glycol) diglycidyl ether (PEO; 0.373 of total polymer) (250 g/1 equivalent epoxide) and pentaerythritol tetrakis (3-mercaptopropionate) (4SH; 0.253 of total polymer) were purchased from Sigma-Aldrich. All materials were used as received. The control and polymer-cement composites were synthesized as previously reported (Table S1) [18]. Briefly, cement samples were synthesized by mixing the class H cement powder (70% of solid powder) and silica flour (30% of solid powder) in a poly(propylene) beaker, then adding deionized (DI) H_2O and mixing to give a cement slurry. To maintain similar rheological properties of the slurry additional water was added when polymers were used so that water to class H cement ratio was 0.54 for control, 0.71 for 10% polymer, and 0.86 for 25% polymer formulations. The slurry was transferred to plastic molds approximately 2.54 cm in diameter by 10.16 cm in length. Molds were placed in a small container and this container inside a larger container containing water and covered in Al foil. This setup was placed inside an oven and the samples were cured at 85 °C for 24 h. Polymer-cement composites were synthesized by adding the monomers mixture to the cement slurry and thoroughly mixing to give polymer-cement slurries (Table S1). Similarly, the polymer-cement mixtures were cured in a high humidity environment at 85 °C for 24 h to simulate the initial temperatures the cement would be exposed to while being pumped into the wellbore. Both cement and polymer-cement composite samples were then removed from the molds and cured in a 2L autoclave vessel with 30 mL of H_2O at 200 °C for an additional 5 days. The higher temperature was selected as an extreme temperature expected to be in a subsurface geothermal setting. The polymer concentration in the polymer-cement composites was 10 wt% for all tests. A polymer-cement composite with 25% polymer by weight of sample was also synthesized to compare with the control cement and the 10 wt% polymer-cement samples in the following analyses; X-ray fluorescence (XRF) microscopy and Full-field X-ray Micro-tomography.

2.2. SEM-EDS

Characterization of polished cement samples (surface roughness < 1 μm) was conducted on a FEI Quanta 600 FEG environmental – scanning electron microscope (FE-SEM) equipped with energy dispersive X-ray spectroscopy (EDS). A backscatter electron (BSE) detector was used to generate images at a working distance of 10 mm and beam spot size of 4 mm with voltages of 10 kV and 20 keV to accommodate sample charging. EDS was used to determine elemental composition. BSE gray-scale intensity coupled with EDS were used to distinguish phases within the cement samples. Brightness in a BSE image is proportional to the average atomic number of a given phase composition [20,21].

To supplement the information provided by the BSE images, EDS was collected at each point identified in the backscattered electron (BSE) images. It is important to note that quantification of carbon and oxygen by EDS is not reliable as its emitted X-rays have low energy and may be absorbed by either the sample specimen or the detector window [22].

2.3. XRF spectroscopy

To prepare for tomography and XRF analysis the cement samples were cut into columns with approximately 2 mm × 2 mm cross section and with a length of 20 mm using a diamond coated wire (~0.5 mm diameter) at low speed. The surface of all four (long) sides of the samples was ground with 600 and 1200 grit silicon carbide papers. Water was used as the cooling fluid in both cutting and grinding/polishing. After grinding, a 1 μm lapping film was used on the flat surfaces, again using water as cooling fluid. No oils or solvents were used to avoid contamination. The polishing was done rapidly and at low temperature, so the assumption was made that minimal geochemical alterations would have occurred to the polished surface. The XRF maps were collected at the SRX beamline (5-ID) in the National Synchrotron Light Source II (NSLS-II) in Brookhaven National Laboratory [23,24]. The energy of the incident beam was 9.6 keV, with the beam size of 1 × 1 μm2. The use of a synchrotron-based X-ray source allowed for ~1 μm^2 resolution, but a 5 μm scanning step size was used in both lateral and vertical directions because it was better suited to the scale of elemental distributions or interest.

2.4. XMT

Tomography of cement samples were conducted at both Environmental and Molecular Sciences Laboratory (EMSL; Richland WA) and at the SRX Beamline (Brookhaven NY). At EMSL a Nikon XTH 320/225 X-ray CT instrument was used to obtain 3D volume data at up to 20–50 μm resolution on sections of cement cores (depending on specimen size), which can then be viewed as sliceable images on the computer and analyzed for structural and density changes. X-ray computed tomography (XCT) images of each piece were collected at high resolution, so that each exposed and unexposed sample could be compared. The 3D data on the cement was then processed in ImageJ (ImageJ: Image Processing and Analysis in Java. Available from: http://imagej.nih.gov/ij/(2017)) to enhance contrast, and the density or structural changes were emphasized with the WEKA segmentation tool in ImageJ/Fiji. The different colors of the segmentation classes' show were the treatment effects the samples.

Full-field tomography experiments were conducted at the SRX Beamline (5-ID, NSLS-II). A monochromatic X-ray beam with 20 kV energy was selected using Si (111) double-crystal monochromator. A total of 1441 image projects were collected on the sample in each tomographic measurement, over 180° angular range (0.125° step size), using pco.edge 5.5 CMOS camera. The images were corrected by dark field images, normalized by white field images, and then aligned using a tomographic data collected on a calibration pin to remove the systematic lateral and vertical displacements.

Tomographic reconstruction of SRX Beamline data was conducted with filtered back projection algorithm using TomoPy, a python based software [25] to reconstruct each set of projections into a 3-dimensional (3D) tomographic dataset. Each reconstructed 3D XCT image dataset was cropped to a volume of 665 × 715 × 880 pixels (Each voxel size is 2.03 × 2.03 × 3 μm) for analysis. A median filter-based smoothing algorithm was then applied to the reconstructed 3D images in freeware Image J [26]. Segmentation was conducted with a thresholding value determined from the histogram of reconstructed images. Ring and streak artifacts [27] in the segmented 3D images were removed in software Avizo (v.9.0, FEI). The artifact removed 3D images were imported to ImageJ for measuring porosity by voxel counting and to dragonfly software (v.2.0, ORS) for analyzing the pore/particle size distribution. The 3D volume visualization was conducted in Avizo.

2.5. Specific surface area analysis

Samples were broken and sieved to 0.5–1 mm diameter fraction before analysis for specific surface area. Surface area was determined using the Micrometrics Surface Area Analyzer, (Model 2020 Micrometrics Instrument Corp., Norcross, Ga). The approach is based on the multi point Brunauer–Emmett–Teller (BET) adsorption equation using nitrogen. A detailed description of the procedure to determine surface area is presented in the operating manual (Micromeritics, 2006). Briefly, an air-dried sediment sample, which will provide at least ten square meters of total surface area, is placed in a surface area flask and out gassed for a minimum of 3 h at 150 °C and at 3 μm Hg. The out gassing temperature was chosen to minimize altering the surface structure as discussed by Davis and Leckie [28]. During this time, physiosorbed water and volatile organics are removed. To determine dryness, the vacuum pumps were isolated and if a vacuum change of less than 2 μm Hg in 5 min occurred, the sample was considered clean and dry. After out gassing, the adsorption isotherm of nitrogen at −196 °C is used to determine the surface area of the sample. The equipment uses an imbalance of atomic forces on the surface of a clean evacuated solid to attract gas molecules. The gas molecules collide with the surface of the sediment and either bounce off or adsorb onto the surface. When the molecules leave the bulk gas to adsorb onto the sediment surface, the number of molecules in the gas decreases, thus the gas pressure decreases. By knowing the temperature, volume of the container, and the change in pressure, the number of molecules adsorbed can be determined. From the number of adsorbed molecules, the surface area can be calculated.

2.6. Compressive strength

Cement monoliths with an average length of 8.2 cm (± 0.5) and diameter of 2.5 cm (± 0.03) were tested for compressive strength using standard methods (ASTM C39/C39M-15a). Before conducting tests, the monolith ends were cut, using a rock saw, perpendicular to the length to provide a flat surface minimizing point loading during tests. Tests were performed using an MTS model 312.31 servohydraulic frame with a 55-kip actuator and load cell. The loading rate was 0.24 MPa/s and cardboard shims were placed between the plate and sample on both ends to absorb potential point loading from sample defects that could increase the risk of test failure. Tests were conducted in triplicate for each condition tested.

2.7. Young's modulus

To calculate Young's Modulus, stress and strain were measured during mechanical testing of the specimens. Tests were performed using an MTS 312.21 servohydraulic universal test frame controlled by Instron Bluehill 2 software. Samples were spatter painted before testing, creating dark contrasting speckles on light colored surface. Stress-strain data was collected using video capture of compression tests with the prepared samples, measuring movements of speckles relative to each other. Load and displacement data is collected during testing and used to calculate stress and strain in the sample throughout the test. The stress-strain curve generated was used to determine the Young's modulus. The elastic modulus of the sample is the ratio of stress to strain in the sample which was calculated by determining the slope of the curve in the elastic region of the test.

2.8. Computational details

Density-functional calculations have been carried out using the CP2K code [29], using the PBE density-functional [30] with the D2 van der Waals correction [31]. The GTH family of pseudopotentials [32], within the Gaussian plane wave hybrid basis set scheme [33] in which double-ζ Gaussian basis sets [34] and 400 Ry cutoff for the plane wave expansion of the auxiliary charge density were used for the simulations. The Brillouin zone was sampled with only the Γ points in self-consistent calculations.

For the computational investigation in this paper, a simulation cell with 902 (Si, Ca, O, H) atoms and with volumetric mass density of 2.33 g cm^{-3} was adopted based on by a C—S—H model proposed in a previous study [35]. This modified model was used in a recent computational study [19] with good results. A short polymer of 116 (C, H, O, S) atoms [19] was also added between two cement with the polymer representing ~6% in weight (Fig. S1). The equilibrium bulk lattice constants were determined first. The unit cell optimization of the C—S—H polymer complex was started with a 2 ps ab initio molecular dynamics run (NVT, T = 300 K) which was followed by zero temperature calculations, resulting in a volumetric mass density of 2.14 g cm^{-3}. The strain along a direction was introduced by changing the corresponding lattice constant, the stress was then computed by geometry optimization. The elastic constant was then computed by the evaluating the stress-strain response along the Z direction.

3. Results and discussion

3.1. Mineralogy and chemistry

To seal wellbores class G and the chemically identical class H cements are commonly used [36]. For the samples tested in this manuscript class H Portland cement was used which commonly contains 62.9–64.2 wt % of calcium oxide, 21.7–21.9 wt % of SiO_2, 3.2–4.2 wt % of Al_2O_3, 3.7–5 wt % of Fe_2O_3, 1.1–4.3 wt % of MgO, and 2.2–2.4 wt % of gypsum [1]. The primary identifiable crystalline phases in Portland cement include: tricalcium silicate (Ca_3SiO_5), dicalcium silicate (Ca_2SiO_4), tricalcium aluminate ($Ca_3Al_2O_6$), and tetracalcium aluminoferrite ($Ca_4Al_2Fe_2O_{10}$) [1]. Silicate minerals make up over 80 wt % of the cement mass in Portland cement [37]. Based on previously published X-ray diffraction results, the minerals identified when curing cement H with silica flour in a mass ratio 70:30 at 200 °C are the calcium silicate mineral xonotlite [$Ca_6Si_6O_{17}(OH)_2$] and quartz (SiO_2) [18]. Furthermore, the mineral composition is similar for both the control cement and the cement-polymer combination.

An initial investigation of polymer influence on the mineralogy was conducted using scanning electron microscopy (SEM) with energy dispersive x-ray spectroscopy (EDS). Results from SEM analysis display some mineral differences between the base cement and cement composite with 10% polymer added (Fig. 2). Visually brighter (lighter) mineral grains can be seen in the polymer-cement composite compared to the control cement (Fig. 2). These lighter grains are a combination of unhydrated cement and silica flour based on EDS and suggests that the unhydrated cement grains are rich in tetracalcium aluminoferrite as previously described [18]. Unhydrated cement grains appear to be the bright white and have well defined, sharp boundaries. Remnants of unhydrated Portland cement particles are present in nearly all cement pastes and are easily identified in SEM [38]. The $Ca(OH)_2$ is less bright than the cement grains and does not exhibit the sharp boundaries but appears as regions with diffuse outlines. The remaining darker areas are composed of the C—S—H (calcium silicate hydrate; $3CaO{\cdot}2SiO_2{\cdot}4H_2O$) phase. As a result of its varying composition and porosity, backscatter electron (BSE) images for C—S—H phase is not always consistent. Silica gel would normally appear darker than the C—S—H phase shown in this image, and as such were not identified. Pores appear as the lowest signal intensity (black) in the BSE image. Changes in the porosity of the cement samples can be estimated by comparing the gray scale intensity of the BSE images [21,39]. The main chemical difference between the control base cement and the polymer-cement composite was the larger concentration of S and C throughout the polymer-cement sample confirming the presence of the polymer homogeneously distributed in the cement matrix as previously identified [18].

3.2. Porosity

Porosity was investigated both with specific surface area and XCT data (Table 1 and Figs. 3 and 4, Figure S2 and Video 1-3). The pores seen in these images have a similar diameter of 100–150 μm for each of the materials imaged. It is best seen in the 3D microstructure evaluation using XCT that there is an increase in porosity with an increase in polymer concentration (Video 1-3). Please note that in Fig. 3 and Video 1-3 voids filled by air or polymer are not differentiated. However, using image segmentation and an advanced algorithmic measurement of the density shows that many of the void spaces had an apparent density between that of the cement and air. This phase is tentatively identified as polymer. With this tool it is then possible to distinguish the spatial distribution of air filled voids and polymer filled voids (Fig. 4 and figure S2). It can be seen from these figures that most of the voids are partially or completely filled with polymer. It is speculated that although the polymers are evenly distributed across the cement matrix, they tend to nucleate around or inside air voids.

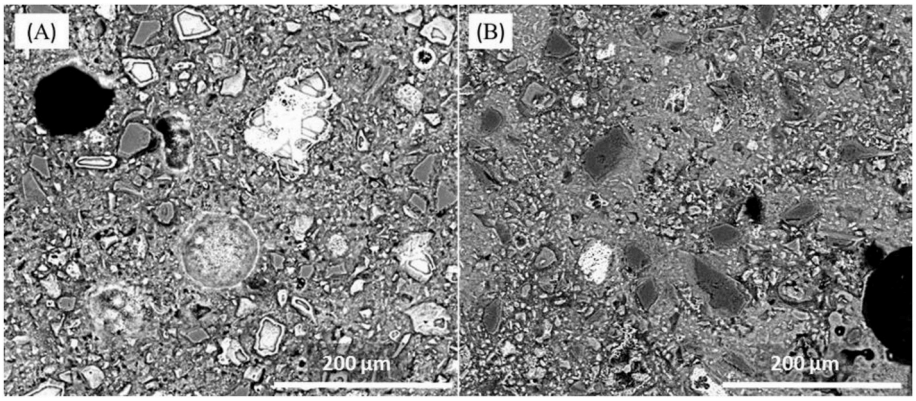

Fig. 2. SEM-BSE images: (A) 10% polymer cement composite; (B) control cement. EDS data was reported in Childers (2017) [18]. Gray matrix is cement paste; White minerals grains are unhydrated cement grains with aluminoferrite; Medium to dark gray grains are silica flour.

Table 1
Specific surface area, volume air void (XCT from EMSL), Young's modulus, and compressive strength results for cement and 10% polymer cement tomography.

Sample	Specific Surface Area ($m^2\ g^{-1}$)	Volume air void (%)	Young's Modulus (GPa)	Compressive strength (MPa)
Control cement	15.9	0.44	11.3 ± *4.9*	47.4 ± *1.5*
10 wt% polymer-cement	16.1	0.22	7.0 ± *1.1*	31.5 ± *4.8*

Supplementary video related to this article can be found at https://doi.org/10.1016/j.cemconcomp.2018.12.022.

Increased polymer concentrations were correlated with the requirement of wider water-to-cement ratios compared to control (base) cement and more porosity. The wider water-to-cement ratio was due to a higher water demand with additional polymer concentration to maintain a slurry with similar consistency to base cement (see Table S1). The fact that there is a larger concentration of voids in the polymer-cement composites observed in XCT images could be due to the presence of excess (unreacted) water during the initial cure of the cement forming pockets or aggregations with the polymers. The water could then evaporate, imbibe into or react with the hardened cement during curing at high temperature (200 °C for 5 days) leaving voids behind. Most of the voids in the hardened cement are filled, partially or completely, by polymer. We hypothesize that the high mobility of the polymers at the curing temperatures allow them to migrate and nucleate at the pockets left behind by the excess water during the cement curing process. Although not a direct measurement of porosity, the specific surface area of the cement could be influenced by the presence of porosity and micro-porosity. The surface area results show that there is little to no difference between the control cement ($15.9\ m^2\ g^{-1}$), and the 10 wt% polymer-cement composite ($16.1\ m^2\ g^{-1}$, Table 1). This could be due to a combination of factors including the cement having low permeability for gas, the pores (voids) are not interconnected, and (in the case of polymer-cement) the existing pores are filled with polymer. Each of these factors could contribute to the similar specific surface area measurements. Based on XCT data it is observed that the polymers do fill these voids and that the voids seem to have no connectivity (Fig. 4). Since most of the voids formed during the curing process in the polymer-cement composite are filled with polymer the total volume of air void is lower (0.22% of the total volume) than the total volume of air void for control cement (0.44% air void) (Table 1).

To validate that the voids correlated to polymer added to composite, analysis of XCT images was used (Fig. S2). Assuming a polymer density of 1 g/mL the polymer content estimated from the 3D XCT images (Fig. S2) for 10 wt% polymer-cement composites was 11.4 wt%. Similarly, the 25 wt% polymer-cement composites showed 20.4 wt% of polymer. The calculated values are highly correlated (r = 0.98) with variability likely the result of human error in mixing the cement or sample variability.

The polymer-cement composites also showed larger concentration of high density unhydrated cement grains throughout the material (Fig. 3). As described earlier, SEM-EDS analysis combined with Fe-based XRF analysis suggest that these unhydrated cement grains are rich in aluminoferrite-based minerals and surprisingly increases with the amount of water relative to cement initially added to these mixtures. This could be explained by the polymer acting as a barrier (retarder) for the hydration of cement increasing the amount of unhydrated silicate minerals in the matrix. Furthermore, rheology analysis showed that cement slurries in the absence of polymer or retarder solidify in less than 30 min at 85 °C while when adding a commercial retarder (calcium lignosulfonate) or 10 wt% of the polymer, the slurry

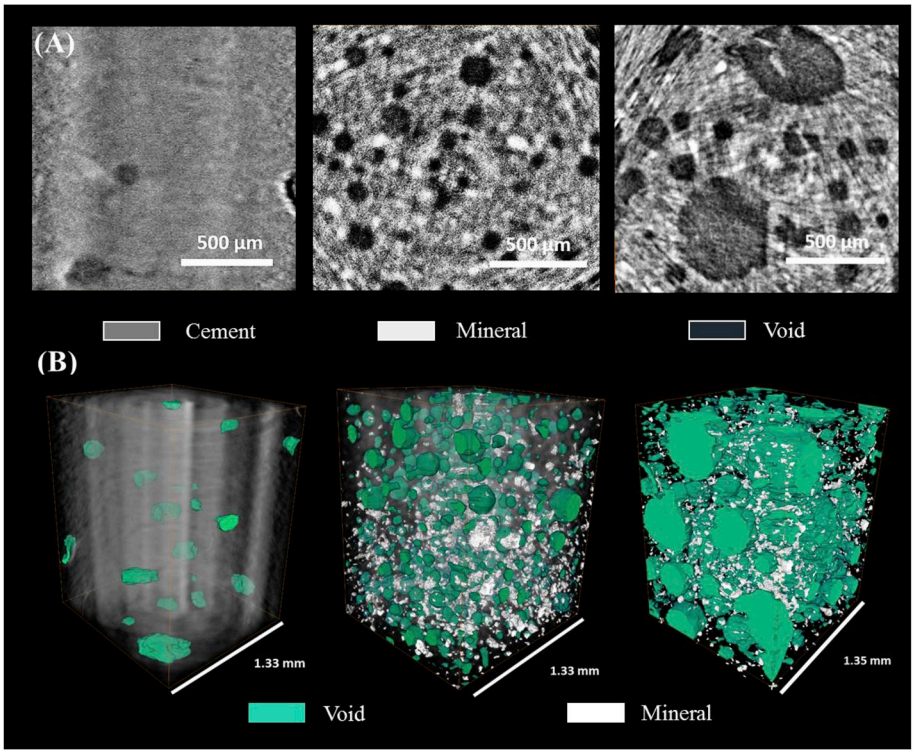

Fig. 3. X-ray tomography (XCT) of pure cement (left) and 10 wt% (middle) and 25 wt% (right) polymer-cement composite samples. (A) 2D XCT of cement and cement composites; (B) 3D XCT with false color classifications of cement and cement composites where gray outline depicts cement sample dimensions, green depicts void space in the samples, white depicts dense unhydrated cement grains rich in aluminoferrite. (For interpretation of the references to color in this figure legend, the reader is referred to the Web version of this article.)

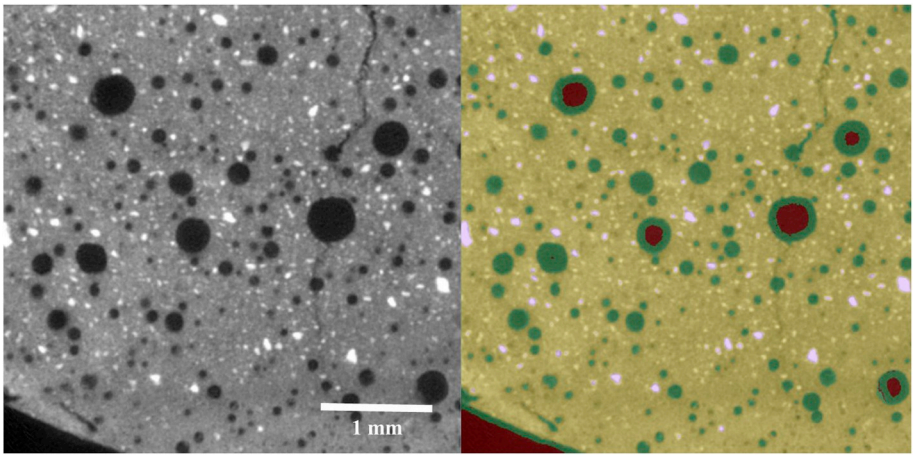

Fig. 4. XCT gray-scale image of 10 wt% polymer-cement composite (left) and colored according to density (right) showing that most void space is filled with polymer, with larger voids being composed of air surrounded by polymer. Cement is colored yellow, unhydrated minerals are white, polymer is medium green, and air is dark red. Note the polymer filled fracture in the top right corner of the image. (For interpretation of the references to color in this figure legend, the reader is referred to the Web version of this article.)

maintain consistency values below 1000 mPa s for 90 min at 85 °C as required for geothermal wellbore cement applications. This demonstrates that the polymer acts as a retarder delaying cement hydration [18]. Similarly, the more flexible polymer filling the pores along with the presence of unhydrated grains possibly explains the lower compressive strength, previously measured [18] on the polymer-cement composites as compared to base cement. It also suggests that the self-healing capability of these polymer-cement composites is associated to the presence of a "reservoir" of latent polymer and uncured (unhydrated) cement ready to flow (polymer) and react in the event of material's damage. The presence of homogeneously distributed polymer throughout the cement matrix seems critical for the self-healing capability of the composite material and its higher ductility as discussed next.

3.3. Element distribution and microstructure

Synchrotron-based X-Ray Fluorescence (XRF) spectroscopic analysis was undertaken to study the elemental distribution of Ca and Fe in the control and polymer-cement composite samples (Fig. 5). Few obvious differences in Ca and Fe distributions are observed between the control cement (Fig. 5a) and polymer cement composites with 10 and 25 wt% polymer concentrations (Fig. 5b and c). Void spaces free of significant amounts of either Ca or Fe tend to increase with the increase of polymer concentration (Fig. 5). In addition, a larger concentration of Ca in the control cement (with dense microstructure and reduced porosity) is observed throughout the sample. Based on the previous findings from X-Ray Diffraction (XRD) analysis, Ca is present in the form of xonotlite [$Ca_6Si_6O_{17}(OH)_2$] with some percentage of gyrolite [$NaCa_{16}$—$Si_{23}AlO_6(OH)_8{\cdot}14H2O$] as the dominant phases [18]. Comparisons of high concentration regions of Ca and Fe demonstrate that they frequently neighbor each other, but they rarely overlap. This is surprising since Fe is expected to be mainly as tetracalcium aluminoferrite minerals [1].

To evaluate if the distribution of Ca and Fe patterns could be explained by presence of voids, XRF images (Fig. 5) were compared to X-ray computed tomography (XCT) micrographs (Fig. 3; Table 2). For this the average diameter of known voids in the XCT were compared to the average diameter of simultaneous low Ca and Fe represented as dark blue regions in the XRF maps (Fig. 5). The sizes were comparable indicating that simultaneous absence of Ca and Fe represented a pore. Similarly, the size of the Fe hot spot (red region) in the Fe XRF was compared with the size of the (unhydrated) white grains from XCT micrographs (Fig. 3, aluminoferrite mineral) showing similar dimensions (Table 2). Nevertheless, the XRF-based sizes for both, voids and unhydrated cement grains, generally had a narrow range compared to the sizes obtained from XCT images mainly due to the smaller area of sample analyzed (Table 2, Fig. 5). The size range for voids from XRF maps for control cement is 70–80 μm which was within the range of voids size obtained from XCT micrographs in control cement samples (60–240 μm). The voids for the 10% and 25% cement polymer composites had ranges of 64–212 μm and 40–160 μm based on XRF maps which were also within the range of the voids observed in XCT polymer-cement samples (Fig. 3, Table 2). When comparing the high concentration iron regions in XRF (red spots), the size range for these spots was 18–53 μm while the size range of the white grain fragments measured on XCT were 20–100 (Table 2, Fig. 3). The larger range found on XCT could, once again, could be due to the larger sample area imaged during XCT analysis as compared to the areas analyzed by XRF. Based on this evidence, it is reasonable to speculate that the simultaneous absence of Fe and Ca in the XRF maps (dark blue regions) correspond to actual sample voids and the red regions in Fe-XRF maps are likely unhydrated minerals (predominantly aluminoferrite-based minerals).

3.4. Mechanical properties

Wellbore cements can be subject to mechanical stresses due to operational and natural process. Mechanical properties were tested using 1) compressive strength analysis, a measure of resistance to breaking under force, and 2) Young's modulus analysis, a measure of tensile elasticity of materials, for both the control cement and 10 wt% polymer-cement composites (Table 1 and Videos 4-9). The compressive strength for the control cement was significantly higher (47.4 ± 1.5) than that of the 10 wt% polymer samples (31.5 ± 4.8 MPa; Table 1). It was previously reported that both the added polymer and associated additional water content which is added with the polymer contribute to the expected decrease in compressive strength [18]. The porosity increase associated to the excess water added in the polymer-cement slurries is the main responsible for the lower compressive strength of the composite materials. Nevertheless, both of these formulations are above the strength value required for geothermal well cement standards (3.5 MPa) [40].

Supplementary video related to this article can be found at https://doi.org/10.1016/j.cemconcomp.2018.12.022.

Tensile elasticity measured by Young's modulus analysis yielded values of 11.3 ± 4.9 GPa for the control cement and 7.0 ± 1.1 GPa for the polymer-cement composites (Table 1). But as important, the strain map (as a function of stress applied) used to generate these Young

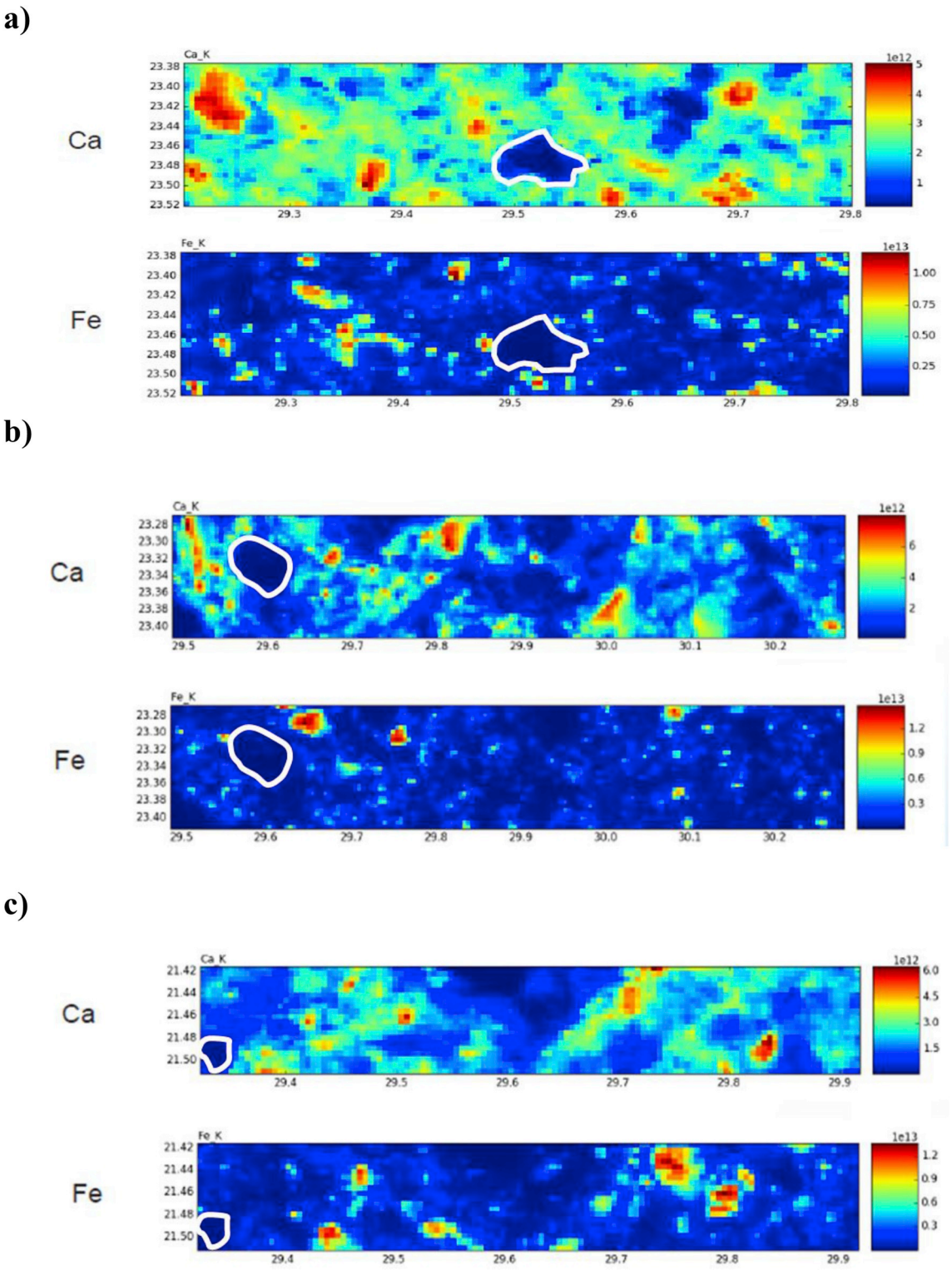

Fig. 5. XRF map of Ca and Fe on one surface of sample for: a) control cement (map dimension = 600 μm by 150 μm); b) 10% polymer cement (map dimension = 800 μm by 150 μm); c) 25% polymer cement composite (map dimension = 600 μm by 100 μm). All with a 5 μm step size. Scale depicts relative intensity of element with red as most concentrated and dark blue as least concentrated. To provide an example of voids measured a white polygon outlines a void (dark blue) in the same location on both Ca and Fe for each map. (For interpretation of the references to color in this figure legend, the reader is referred to the Web version of this article.)

modulus values, showed some differences between control cement and polymer-cement composite samples. The strain map for the control cement samples consistently showed a heterogeneous distribution of strain as a function of stress applied throughout the entire course of the test (Video 4-6). On the other hand, the strain maps of the 10 wt% polymer-cement composites at any given applied pressure showed a more homogeneous distribution of strain in the entire sample, which also uniformly increases with stress applied, until the very end where

Table 2
Comparison of diameter range for features from XCT images and XRF element maps of cement and polymer cement composites. Voids measured in this table do not differentiate air filled versus polymer plus air filled.

Data source	Diameter Total Voids (μm)	Diameter Mineral Grains (μm)
XRF control	70–80[b]	18–38[c]
XRF 10% polymer	64–212[b]	28–53[c]
XRF 25% polymer	40–160[b]	24–44[c]
XCT control	60–240[a]	Not measured
XCT 10% polymer	40–500[a]	20–100[a]
XCT 25% polymer	60–500[a]	20–100[a]

[a] Diameters measured from 2D XCT images.
[b] Diameter for void estimated from XRF by measuring across areas of simultaneous low Ca and Fe concentration.
[c] Diameter for mineral grains estimated from XRF by measuring across areas of high Fe relative concentration (unhydrated cement, aluminoferrite).

mechanical failure occurs (Video 7-9). We hypothesize that this is due to the polymer-cement composites being relatively more elastic/ductile than pure cement samples which allow them to better respond against mechanical stress.

Recent models show that the overall elasticity and healing properties of these composites stem from a flexible hydrogen bonding network that can readily adapt to surface morphology [19]. This elasticity is further investigated here where Fig. 6 shows the computed stress-strain data. In the strain range studied, an almost linear stress/strain response is seen, corresponding to the elastic portion of the stress-strain curve. For the pure cement sample, a value of 80 GPa was estimated for the Young's modulus compared to the experimental value of 11.3 ± 4.9 GPa. For the polymer-cement composite, the computed value of the Young's modulus is 23 GPa compared to the experimental value of 7.0 ± 1.1 GPa. Here, it is important to point out that the absolute theoretical values of the elastic moduli are expected to be considerably higher than the experimental ones because the models lack the micro and meso-porosity of the actual materials. The reason for this is that it is not possible to build a molecular model that simultaneously represents the surface chemistry [at the Density Functional Theory (DFT) level] and also captures the porosity of the real system that is manifested at a larger length-scale. Nevertheless, our molecular models have been tested and are able to represent the relative changes [41] to the elasticity after the addition of the polymer and follow the same trends as the experimental measurements. The data in Fig. 6a show that the modulus of elasticity in the cement-polymer is about a third of the pure cement, hence, becoming approximately 70% more elastic compared to about 63% estimated from the experimental values. This change is also reflected in the changes of the volumetric specific mass density, which becomes 2.14 g cm^{-3} after the addition of the polymer, compared to 2.33 g cm^{-3} in the pure cement (see Method section). These changes in density are associated to the presence of a less dense polymer as well as to the higher porosity. The latter is likely to stem from the evaporation and/or absorption of excess (unreacted) water in the cement, while the overall flexibility of the polymer also increases the ductility of the composite system.

Finally, it was previously reported that the chemical interactions between the polymer and cement are dominated by polymer/C—S—H hydrogen bonding [19,42]. The potential energy surfaces for these interactions are soft such that large deformations can be accommodated without compromising the bonding interactions [19,42]. As seen in Fig. 6b, the number of hydrogen bonds remain approximately the same over the range of strain considered in this work.

4. Conclusion

As demonstrated in this manuscript the topological and elemental structure of cements can be adjusted and correlated with the formulation composition, in particular, water-to-cement ratio and polymer concentration. The resulting mechanical properties are also heavily affected by these two parameters. Control cements without polymer are well cured and possess small void spaces with low levels of uncured cement grains. Polymer-cement composites have relatively larger, though not interconnected, levels of void spaces mostly filled with polymer. The composites also seem to have higher levels of uncured cement grains as the polymer seems to act as a retarder in the cement curing process. It is hypothesized that the excess water added to prepare the slurry in the polymer-cement composites is responsible for the higher porosity since at the high curing temperatures (200 °C) excess water either (or both) evaporates or further react/imbibe into the cement matrix leaving pockets behind. The fact that the majority of these pockets are filled with polymer has to do with the high mobility of the polymer at these curing temperatures, migrating and nucleating in the void spaces generated. The lower compressive strength measured in the polymer-cement composites is primarily associated to the higher porosity of the composite materials. Nevertheless, the compressive strength values (31.5 MPa) are significantly higher than the required values for geothermal well cement standards (3.5 MPa). The presence of homogeneously-distributed more flexible polymer in the cement brings about 60–70% higher tensile elasticity to the composite material, as confirmed experimentally and by density-functional calculations. The significantly higher tensile elasticity renders more ductility to the composite material. Cement ductility, together with the recently reported self-healing capability [18], are of critical importance to reduce the formation/propagation of fractures as a result of mechanical stress. The application of these cement-polymer composites in geothermal wellbores should then reduce/minimize the environmental and economic issues associated to wellbore failure and intervention.

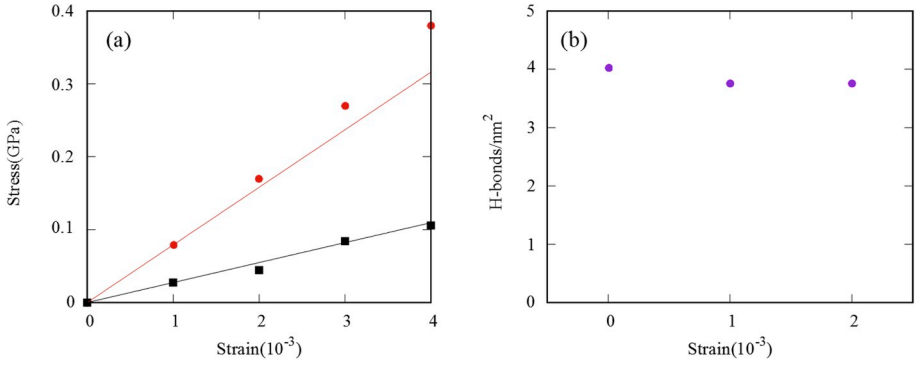

Fig. 6. Strain plots from simulation: a) stress vs. strain from simulation for base cement (red plot) and 10 wt% polymer-cement (black plot): points indicate computed data; solid straight lines are fitted from these data. Bulk compression was considered; b) number of hydrogen bonds in polymer-cement composite relative to strain from simulation. (For interpretation of the references to color in this figure legend, the reader is referred to the Web version of this article.)

Acknowledgements

Funding provided by the Department of Energy's Geothermal Technology Office. PNNL is operated by Battelle for the U.S. DOE under Contract DE-AC06-76RLO 1830. Work at Brookhaven National Laboratory was performed using funding from Laboratory Directed Research and Development (LDRD) Program under project no 16-019. Part of this research was performed at the W.R. Wiley Environmental Molecular Sciences Laboratory (EMSL), a national scientific user facility at PNNL managed by the Department of Energy's Office of Biological and Environmental Research, and simulations were performed using PNNL Institutional Computing. This research used resources of the National Energy Research Scientific Computing Center, a DOE Office of Science User Facility supported by the Office of Science of the U.S. Department of Energy under Contract No. DE-AC02-05CH11231. This research used resources and SRX beamline (5-ID) of the National Synchrotron Light Source II, a U.S. Department of Energy Office of Science User Facility operated for the DOE Office of Science by Brookhaven National Laboratory under Contract No. DE-SC0012704. K. Chen-Wiegart and C Zhao acknowledge the support by the Department of Materials Science and Chemical Engineering, the College of Engineering and Applied Sciences, and the Stony Brook University, as well as by the Brookhaven National Laboratory under Contract No. DE-SC0012704.

Appendix A. Supplementary data

Supplementary data to this article can be found online at https://doi.org/10.1016/j.cemconcomp.2018.12.022.

References

[1] E.B. Nelson, D. Guillot (Eds.), Well Cementing, second ed., Schlumberger, Sugar Land, TX, 2006.
[2] R. Shortall, B. Davidsdottir, G. Axelsson, Geothermal energy for sustainable development: a review of sustainability impacts and assessment frameworks, Renew. Sustain. Energy Rev. 44 (2015) 391–406.
[3] R. Kiran, C. Teodoriu, Y. Dadmohammadi, R. Nygaard, D. Wood, M. Mokhtari, S. Salehi, Identification and evaluation of well integrity and causes of failure of well integrity barriers (A review), J. Nat. Gas Sci. Eng. 45 (2017) 511–526.
[4] A.N. Zeldin, L.E. Kukacka, N. Carciello, Polymer-cement-geothermal-well-completion Materials, Brookhaven National Laboratory/U.S. Department of Energy, Washington, DC, 1980.
[5] T.J. Rockett, E.E. McEwen, J.P. Clappin, S.S. Feng, A.J. Ouellette, N.C. Thakore, S.J. Yuh, Phosphate-bonded Glass Cements for Geothermal Wells, BNL 51153, Brookhaven National Laboratory/U.S. Department of Energy, Washington, DC, 1979.
[6] T. Sugama, Advanced Cements for Geothermalwells, BNL 77901-2007, Brookhaven National Laboratory/U.S. Department of Energy, Washington, DC, 2006.
[7] K. Van Tittelboom, N. De Belie, Self-healing in cementitious materials-A review, Materials 6 (2013) 2182–2217.
[8] M. Wu, B. Johannesson, M. Geiker, A review: self-healing in cementitious materials and engineered cementitious composite as a self-healing material, Constr. Build. Mater. 28 (2012) 571–583.
[9] P.H. Cavanagh, C.R. Johnson, S.L. Roy-Delage, G.G. DeBruijn, I. Cooper, D.J. Guillot, H. Bulte, B. Dargaud, Self-healing cement - novel technology to achieve leak-free wells, SPE/IADC, SPE/IADC Drilling Conference, Amsterdam, The Netherlands, Richardson, TX, 2007.
[10] B.R. Reddy, F. Liang, R.M. Fitzgerald, D. Meadows, Self repairing cement composites and methods of using same, U.S. Patent 7 (530) (2009) 396B1.
[11] B.R. Reddy, F. Liang, R.M. Fitzgerald, Self-healing cements that heal without dependance on fluid contact: a laboratory study, SPE Drill. Complet. 25 (2010) 309–313.
[12] S.L. Roy-Delage, M. Martin-Beurel, K. Dismuke, E.B. Nelson, Self Adaptive Cement Systems, U.S. Patent 8,469,095B2, 2013.
[13] H.X.D. Lee, H.S. Wong, N.R. Buenfeld, Self-sealing of cracks in concrete using superabsorbent polymers, Cement Concr. Res. 79 (2016) 194–208.
[14] W.T. Li, Z.W. Jiang, Z.H. Yang, H.T. Yu, Effective mechanical properties of self-healing cement matrices with microcapsules, Mater. Des. 95 (2016) 422–430.
[15] D. Snoeck, J. Dewanckele, V. Cnudde, N. De Belie, X-ray computed microtomography to study autogenous healing of cementitious materials promoted by superabsorbent polymers, Cement Concr. Compos. 65 (2016) 83–93.
[16] J. Todorovic, M. Raphaug, E. Lindeberg, T. Vralstad, M.L. Buddensiek, Remediation of leakage through annular cement using a polymer resin: a laboratory study, in: R. Aarlien, N.A. Rokke, H.F. Svendsen (Eds.), 8th Trondheim Conference on Co_2 Capture, Transport and Storage, Elsevier Science Bv, Amsterdam, 2016, pp. 442–449.
[17] H.L. Zhao, H.T. Yu, Y. Yuan, H.B. Zhu, Blast mitigation effect of the foamed cement-base sacrificial cladding for tunnel structures, Constr. Build. Mater. 94 (2015) 710–718.
[18] M.I. Childers, M.T. Nguyen, K.A. Rod, P.K. Koech, W. Um, J. Chun, V.A. Glezakou, D. Linn, T.J. Roosendaal, T.W. Wietsma, N.J. Huerta, B.G. Kutchko, C.A. Fernandez, Polymer-cement composites with self-healing ability for geothermal and fossil energy applications, Chem. Mater. 29 (2017) 4708–4718.
[19] M.T. Nguyen, Z.M. Wang, K.A. Rod, M.I. Childers, C. Fernandez, P.K. Koech, W.D. Bennett, R. Rousseau, V.A. Glezakou, Atomic origins of the self-healing function in cement-polymer, Compos. ACS Appl. Mater. Interfaces 10 (2018) 3011–3019.
[20] P.E. Stutzman, J.R. Clifton, Specimen preparation for scanning electron microscopy, Proceedings of the 21st International Conference on Cement Microscopy, International Cement Microscopy Association, Las Vegas, NV, 1999, pp. 10–22.
[21] N. Thaulow, S. Sahu, S.R. Badger, Identification of phases in cement and concrete using backscattered electron imaging, Proceedings of the 24th International Conference on Cement Microscopy, International Cement Microscopy Association, San Diego, CA, 2002, pp. 214–223.
[22] P.T. Durdzinski, C.F. Dunant, M. Ben Haha, K.L. Scrivener, A new quantification method based on SEM-EDS to assess fly ash composition and study the reaction of its individual components in hydrating cement paste, Cement Concr. Res. 73 (2015) 111–122.
[23] Y.C.K. Chen-Wiegart, G. Williams, C.H. Zhao, H. Jiang, L. Li, M. Demkowicz, M. Seita, M. Short, S. Ferry, T. Wada, H. Kato, K.W. Chou, S. Petrash, J. Catalano, Y. Yao, A. Murphy, N. Zumbulyadis, S.A. Centeno, C. Dybowski, J. Thieme, Early science commissioning results of the sub-micron resolution X-ray spectroscopy beamline (SRX) in the field of materials science and engineering, in: J. Thieme, D.P. Siddons (Eds.), Icxom23: International Conference on X-Ray Optics and Microanalysis, 2016.
[24] Y.C.K. Chen-Wiegart, G. Williams, J. Thieme, https://www.bnl.gov/ps/beamlines/beamline.php?b=SRX, Brookhaven National Laboratory.
[25] D. Gursoy, F. De Carlo, X.H. Xiao, C. Jacobsen, TomoPy: a framework for the analysis of synchrotron tomographic data, J. Synchrotron Radiat. 21 (2014) 1188–1193.
[26] C.A. Schneider, W.S. Rasband, K.W. Eliceiri, NIH Image to ImageJ: 25 years of image analysis, Nat. Methods 9 (2012) 671–675.
[27] J.F. Barrett, N. Keat, Artifacts in CT: recognition and avoidance, Radiographics 24 (2004) 1679–1691.
[28] J.A. Davis, J.O. Leckie, Surface ionization and complexation at oxide-water interface. 2. Surface propertire of amorphous iron oxyhydroxide and adsorption of metal-ions, J. Colloid Interface Sci. 67 (1978) 90–107.
[29] J. VandeVondele, M. Krack, F. Mohamed, M. Parrinello, T. Chassaing, J. Hutter, Quickstep: fast and accurate density functional calculations using a mixed Gaussian and plane waves approach, Comput. Phys. Commun. 167 (2005) 103–128.
[30] J.P. Perdew, K. Burke, M. Ernzerhof, Generalized gradient approximation made simple, Phys. Rev. Lett. 77 (1996) 3865–3868.
[31] S. Grimme, Semiempirical GGA-type density functional constructed with a long-range dispersion correction, J. Comput. Chem. 27 (2006) 1787–1799.
[32] S. Goedecker, M. Teter, J. Hutter, Separable dual-space Gaussian pseudopotentials, Phys. Rev. B 54 (1996) 1703–1710.
[33] B.G. Lippert, J.H. Parrinello, Michele, A hybrid Gaussian and plane wave density functional scheme, Mol. Phys. 92 (1997) 477–488.
[34] J. VandeVondele, J. Hutter, Gaussian basis sets for accurate calculations on molecular systems in gas and condensed phases, J. Chem. Phys. 127 (2007) 114105.
[35] G. Kovacevic, B. Persson, L. Nicoleau, A. Nonat, V. Veryazov, Atomistic modeling of crystal structure of Ca1.67SiHx, Cement Concr. Res. 67 (2015) 197–203.
[36] J.-P.L. Brunet, L. Li, Z.T. Karpyn, B.G. Kutchko, B. Strazisar, G. Bromhal, Dynamic evolution of cement composition and transport properties under conditions relevant to geological carbon sequestration, Energy Fuel. 27 (2013) 4208–4220.
[37] H.F.W. Taylor, Cement Chemistry, second ed., Thomas Telford, London, UK, 1997.
[38] S. Diamond, The microstructure of cement paste and concrete - a visual primer, Cement Concr. Compos. 26 (2004) 919–933.
[39] B.G. Kutchko, B.R. Strazisar, D.A. Dzombak, G.V. Lowry, N. Thaulow, Degradation of well cement by CO_2 under geologic sequestration conditions, Environ. Sci. Technol. 41 (2007) 4787–4792.
[40] T. Sugama, Advanced Cements for Geothermal Wells, Brookhaven National Laboratory, 2006.
[41] R. Alizadeh, J.J. Beaudoin, L. Raki, Mechanical properties of calcium silicate hydrates, Mater. Struct. 44 (2011) 13–28.
[42] M.-T.W. Nguyen, Zheming, Kenton A. Rod, M. Ian Childers, Carlos Fernandez, Phillip K. Koech, Wendy D. Bennett, Roger Rousseau, Glezakou, Vassiliki-alexandra atomic origins of self-healing function in cement-polymer composites, ACS Appl. Mater. Interfaces 10 (3) (2018) 3011–3019.